

The intriguing bifunctional effect of strong metal support interaction (SMSI) and hydrogen spillover effect (HSPE) for effective hydrogen evolution reaction

R. Rajalakshmi, G. Srividhya, C. Viswanathan, N. Ponpandian *

Department of Nanoscience and Technology, Bharathiar University, Coimbatore 641046, India



ARTICLE INFO

Keywords:

Strong metal-support interaction
Hydrogen spillover effect
Electrochemical water splitting
Hydrogen evolution reaction
Graphene

ABSTRACT

The mechanistic insights behind the kinetics of Hydrogen evolution reaction are unraveled through the bifunctional effect - Strong Metal Support Interaction (SMSI) and Hydrogen Spillover Effect (HSPE) on the WO_3 hexagonal nanorods decorated with gold clusters and supported on the reduced graphene layers. The investigation is extended to scaling the electrocatalyst in a flexible electrode-carbon fiber for robust hydrogen evolution reaction in broad pH spectra. The research found that the proposed electrocatalyst demonstrated a reduced overpotential of 20 mV at a current density of 10 mA cm^2 in acidic conditions and the stability of the ternary catalyst was verified through the Pourbaix profile. The Tafel slope was also comparable to that of the noble metal electrocatalyst Pt/C, with values of 35 mV dec^{-1} in $0.5 \text{ M H}_2\text{SO}_4$. The study demonstrated the potential for large-scale application of the proposed catalyst with stable operation observed for 24 h.

1. Introduction

Hydrogen production from water splitting has been in the spotlight of energy research for the past 20 years, as it stands as an eco-friendly and sustainable solution to the noxious effects of fossil fuel exploitation [1,2]. Weighed among the other process of hydrogen production like steam reforming and thermal processes, water splitting can be accomplished in normal conditions with lower energy. Water splitting is a result of two half-cell reactions, namely hydrogen evolution reaction (HER) where hydrogen is produced at the cathode and oxygen evolution reaction (OER) where oxygen is evolved at the anode. Catalyzing these half-reactions is crucial for easing overall water splitting for efficient hydrogen production for fuel cell applications. Understanding the mechanism behind the function of the electrocatalysts to satisfy these half-cell reactions remains a major challenge, especially in hybrid electrocatalysts consisting of one or more additional components to the primary catalyst.

In recent times, metal-support systems pronounced performance towards HER, with the aid of hydrogen spillover mechanism [3]. Hydrogen spillover effect (HSPE) is the transfer of charges from the surface of metal based catalyst to the surface of the support material. In HSPE aided HER, the protons that are adsorbed on the metal surface are

transferred to the support material's surface where it is readily desorbed as molecular hydrogen. Thus, the combination of the metal-support systems overcomes the non-zero Gibb's free energy for hydrogen adsorption, which is crucial for HER catalysis [4]. The activity and stability of a catalyst could be enhanced immensely when a metal gets interacted on the surface of a catalyst. In HER, the metal possessing exceptional chemical stability, surface, and electronic properties acts as the catalytic site where the hydrogen evolution reaction commences, and the surface material provides a physical and chemical environment for the metal to interact with the electrolyte and the hydrogen species. This is called the strong metal support interaction (SMSI) phenomenon which leads to a higher dispersion of the metal on the surface of the parent catalyst, thereby increasing the number of active sites available for the reaction. Further, metal catalysts with strong metal support interaction (SMSI) have regained research attention, owing to the surge in the development of different support nanomaterials and facile metal-support preparation techniques. Metals like Gold (Au), Platinum (Pt), Palladium (Pd), and Rhodium (Rh), have synergistic interfacial contact with supports resulting in SMSI [5,6]. The strong chemisorption of metals on the supports prevents their agglomeration, thus providing atomic utilization of the metal beneficial for effectively and durably catalyzing HER.

* Corresponding author.

E-mail address: ponpandian@buc.edu.in (N. Ponpandian).

Ideal catalysts for water splitting are based on noble metals like Platinum (Pt) for HER and Ruthenium (Ru) and Iridium (Ir) for OER. Numerous non-noble metal based catalysts have been explored and put forth by the research community for affordable water splitting and understanding the kinetics of SMSI and HSPE [7]. Transition metal oxides are among the top non-noble metal based materials that are widely studied for HER and OER catalysis, owing to their feasibility of tuning different crystallographic structures, oxidation states and morphology, which have a crucial impact on catalytic activity [8]. Mixed phases of hexagonal and monoclinic tungsten oxide (WO_3) exhibited improved HER catalytic activity with a low overpotential of 170 mV at 10 mA cm $^{-2}$ current density, when compared with its single-phase counterparts [9]. WO_3 can be easily modified by simple hydrothermal methods followed by calcination to engineer oxygen vacancies for increased catalytic activity [10]. Morphology is an influential factor in the activity of a catalyst and WO_3 can be easily tuned to have different HER boosting morphologies by simple hydrothermal method, with different structural agents. Doping foreign atoms and compositing with support materials are prominent strategies to augment the catalytic activity of WO_3 [11].

Two dimensional carbon-based nanomaterials like graphene, graphene oxide (GO), reduced graphene oxide (rGO), reduced graphene (GR), and carbon black (CB) to name a few, are the most suited candidates as catalysts support materials to study the principle of HSPE [12]. They have unique electronic structures, high conductivity, high mechanical strength and enlarged surface area, all of which bolster the performance of the catalyst material. Noble metals (Au, Ag, Pt, Pd, etc.,) doping and decoration strategy has been profoundly investigated for the correlation of interaction with the metal surface on which it is decorated. This aids to understand the intensity of electron density useful to understand the reaction kinetics involved in Strong Metal Support Interaction (SMSI) [6,13].

In the present work, HSPE combined with the SMSI mechanism is studied for the first time with the aid of a ternary nanohybrid - $\text{WO}_3/\text{GR}/\text{Au}$. The WO_3/GR interface stimulates HSPE whereas the WO_3/Au interface promotes SMSI for outstanding HER activity which is on par with the state of art electrocatalyst - Platinum. The stability of the electrocatalyst is also detailed through 2D and 3D Pourbaix stability plots to substantiate the durability of the electrocatalyst in a wide pH range.

2. Experimental procedures

2.1. Chemicals

Sodium tungstate dihydrate ($\text{Na}_2\text{WO}_4 \cdot 0.2 \text{ H}_2\text{O}$) (purity $\geq 99.9\%$), commercial Pt/C (20 wt%), Gold(III) chloride trihydrate ($\text{HAuCl}_4 \cdot 3 \text{ H}_2\text{O}$) ($\geq 99.9\%$ trace metals basis), and carbon cloth fibers (CC) were purchased from Sigma and used as received. Hydrochloric acid (HCl), Oxalic acid, Potassium hydroxide pellets (KOH), Lithium Sulphate (Li_2SO_4), Graphite flakes, Carbon black, Hydrazine hydrate ($\text{NH}_2\text{NH}_2 \cdot x\text{H}_2\text{O}$), and Absolute Ethanol (99.9%) ($\text{C}_2\text{H}_5\text{OH}$) were procured from Hi-Media. Sulphuric acid (95–97% purity) (H_2SO_4) was purchased from Merck. Deionized (DI) water was used for the electrocatalyst synthesis and also for the preparation of catalyst ink and electrolyte solution.

2.2. Synthesis

2.2.1. Synthesis of hexagonal WO_3 nanorods

WO_3 nanorods were synthesized by following the procedure described in [1]. Briefly, 1 M $\text{Na}_2\text{WO}_4 \cdot 2 \text{ H}_2\text{O}$ (1 M) was introduced into 50 ml DI and stirred to attain a homogeneous solution. The pH of the solution was brought down to 1 using citric acid and HCl solution. 3 g of Li_2SO_4 was used as a structure-directing agent. The final precursor solution was sealed at 180 °C for 10 hrs. The powder obtained was washed several times with water and ethanol and dried at 100 °C overnight.

Finally, calcination for 3 hrs at 450 °C was initiated to obtain WO_3 nanorod powders.

2.2.2. Synthesis of WO_3 nanorods with carbon entities - GO, rGO, and GR

Graphene oxide (GO) was prepared using graphite flakes by a modified Hummer's method reported earlier [14]. To derive reduced graphene oxide (rGO) from the synthesized GO, a chemical exfoliation technique was utilized where 20 mg of GO was dispersed along with 1 vol% of hydrazine hydrate solution and refluxed at ~ 100 °C for 2 hrs. The WO_3/GO electrocatalyst was synthesized by ultrasonication for 2–3 hrs with 20 mg of the synthesized GO powder with 80 mg of WO_3 nanorod powder sample. To prepare the WO_3/rGO electrocatalyst, the same amount of GO powder was introduced into the Teflon autoclave comprising the final homogeneous solution of WO_3 precursors and sealed for 10 hrs at 100 °C. The WO_3/GR electrocatalyst was further obtained by thermal expansion where the WO_3/rGO powders after washing and drying at room temperature were introduced into a quartz tube to attain a temperature of 300 °C along with argon gas purged into it. This splits the reduced graphene oxide into multiple layers of reduced graphene sheets through the evolution of CO_2 . The WO_3/CB electrocatalyst was obtained by ultrasonication of the specified amount of CB powders with the pristine WO_3 electrocatalyst as mentioned for WO_3/GO powders.

2.2.3. Synthesis of Au supported on $\text{WO}_3/\text{carbon hybrids}$

To decorate the WO_3 nanorod composites with Au, primarily 100 mg of the respective WO_3 binary composite sample was introduced into 10 ml DDW and dispersed well by sonication. Further to the solution, 10 ml of 0.01 M HAuCl_4 was added and stirred for an hour to attain a homogeneous solution. Finally, 0.5 ml of 1 M hydrazine hydrate which acts as a reducing agent was added dropwise with continuous stirring. The Au nanoparticles were formed and decorated onto the surface of the WO_3 nanorods and the respective carbon composites which resulted in a precipitate formation. Finally, the residue was rinsed multiple times with water and ethanol and dried to obtain the respective Au-decorated WO_3 hybrid electrocatalysts - $\text{WO}_3/\text{GO}/\text{Au}$, $\text{WO}_3/\text{rGO}/\text{Au}$, $\text{WO}_3/\text{GR}/\text{Au}$, and $\text{WO}_3/\text{CB}/\text{Au}$.

2.2.4. Synthesis of $\text{WO}_3/\text{GR}/\text{Au}$ nanohybrids on CC and SS substrates

To fabricate the CC@ $\text{WO}_3/\text{GR}/\text{Au}$ electrode, carbon cloth fiber measuring 1×1 cm as the working dimension was introduced into the Teflon autoclave and the hydrothermal protocol was repeated for the WO_3/GO electrocatalyst. The rinsing and calcination steps were the same as discussed above to obtain CC@ WO_3/GR electrode. The electrode procured after the synthesis was subjected to ultrasonication in the reduced Auric chloride solution containing 1 wt% of the Au precursor and further rinsed multiple times with water and ethanol to remove the chloride ions to obtain the CC@ $\text{WO}_3/\text{GR}/\text{Au}$ working electrode. To fabricate the SS@ $\text{WO}_3/\text{GR}/\text{Au}$ electrode, the $\text{WO}_3/\text{GR}/\text{Au}$ powder electrocatalyst was made into a slurry using Nafion and ethanol and smeared on the SS substrate with the same $1 \times 1 \text{ cm}^2$.

2.3. Physical characterization

X-ray diffraction (XRD) (RigakuUltima 1 V X-ray Diffractometer with Cu-K α radiation ($\lambda = 1.5406 \text{ \AA}$) was performed to derive the crystallographic information of the synthesized hybrid electrocatalysts. A Horiba JobinYvon, LabRam-HR Raman spectrometer was used to determine the Raman spectra using a 514 nm laser. A ULVAC-PHI, PHI5000 Version Probe III was used to understand the oxidation states and chemical surface composition through X-Ray absorption spectroscopy (XPS). An FEI, QUANTA 250-FEG was utilized as a field-emission scanning electron microscope to scan the surface morphology of the electrocatalysts. The structural information investigation, chemical compositions, and elemental mapping of samples were probed by a TEM (JEOL, JEM-2100) and HR-TEM (JEOL, JEM-2100 F). The absorbance

and bandgap calculations were determined by a UV-vis spectrophotometer (UV-2550, Japan). The specific surface area and pore size distribution were interpreted using Brunner-Emmett-Teller (BET) analysis (Microtrac, BELSORP-max).

2.4. Electrode preparation and electrochemical measurements

The preparation of catalyst inks includes 5 mg of ultrasonically dispersed catalyst into ethanol and Nafion solution (DuPont, 0.5 wt%) (8:2) ratio for 30 mins. A catalyst loading mass of 0.36 mg cm^{-2} where 5 μL of catalyst inks (5 mg mL^{-1}) loaded to the glassy carbon electrode GCE surface (3 mm in diameter) was pre-polished priorly with an exposed area of 0.07 cm^2 .

Electrochemical measurements were performed with a PARSTAT electrochemical workstation in a standard three-electrode system comprising the respective electrocatalyst coated on the GCE /CC/SS substrate as the working electrode, a graphite rod as the counter electrode, and a saturated calomel electrode as the reference electrode. The

electrolyte solutions taken for the study ($0.5 \text{ M H}_2\text{SO}_4$, pH = 0 and 1 M KOH , pH = 14) were purged with Ar gas for 30 mins before measurements. In all measurements, the potential was converted with respect to Reversible Hydrogen Electrode (RHE) according to the Nernst equation:

$$E_{\text{RHE}} = E_{\text{SCE}} + E^\circ_{\text{SCE}} + 0.059 \times \text{pH} \quad (1)$$

where E_{RHE} describes the experimentally measured potential and E_{SCE} denotes the standard potential of saturated calomel electrode.

For the cathodic measurements, $\sim 50 \text{ CV}$ (cyclic voltammetry) cycles were performed to attain a stable polarization curve before each LSV (linear sweep voltammetry) curve was measured. The measurements of the HER polarization curve were performed with LSV at a scan rate of 5 mV s^{-1} and stability tests were performed under their respective constant overvoltage values for a period of 16 h.

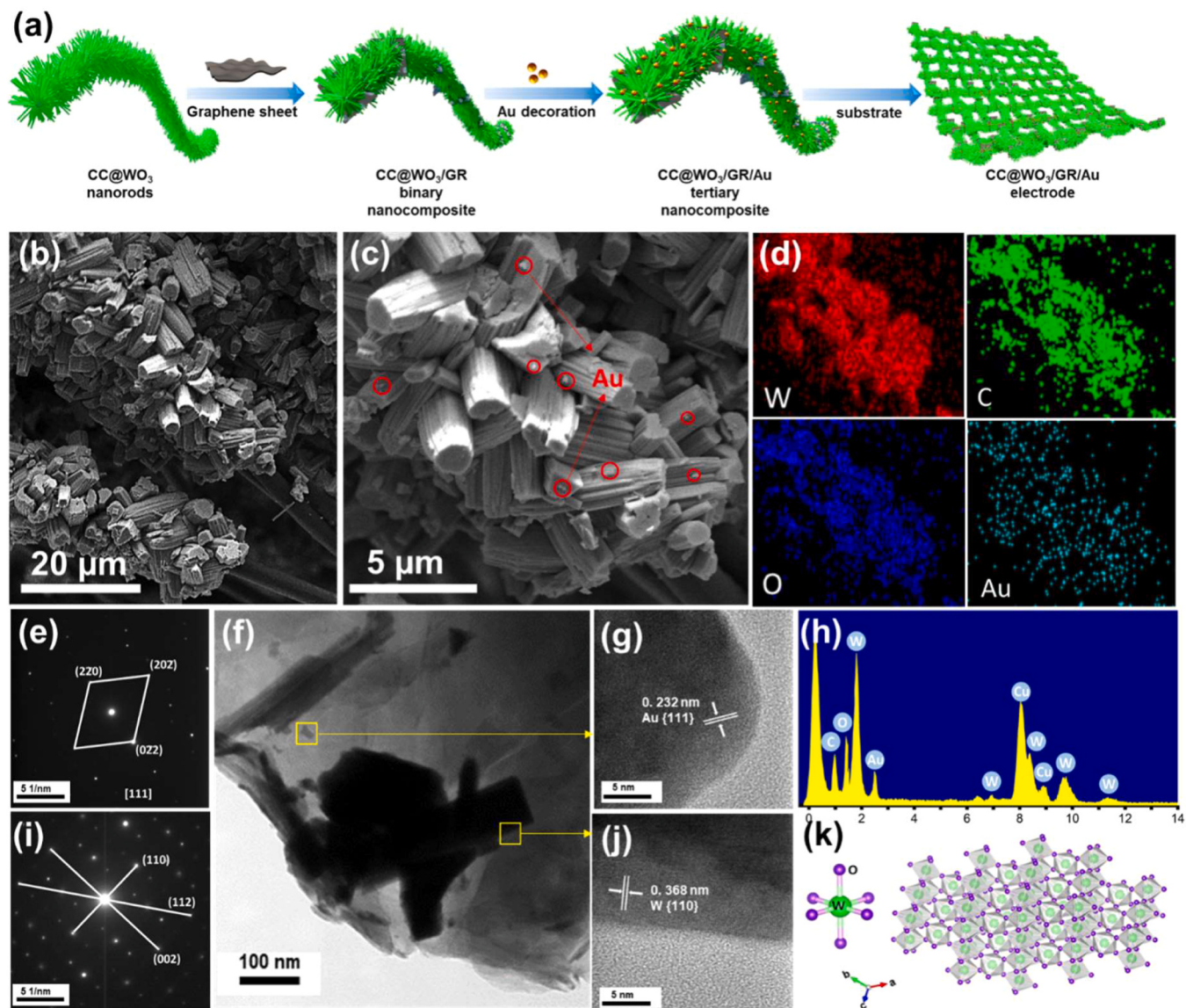


Fig. 1. (a) Illustration of the hydrothermal synthesis of WO_3 hexagonal nanorods and their respective nanocomposite formation on carbon cloth substrate, (b) FESEM image of $\text{WO}_3/\text{GR}/\text{Au}$ ternary nanocomposite grown on CC fiber, (d) the enlarged morphological analysis of the ternary nanocomposite depicting the Au nanoclusters, (d) the respective elemental composition of W, C, O and Au, (e) SAED pattern of Au representing the hkl planes, (f) The TEM image of $\text{WO}_3/\text{GR}/\text{Au}$ electrocatalyst, (g) the interplanar distance in nm of Au (111) plane, (h) The EDS mapping confirming the presence of the elements in the composite, (i) SAED pattern of W representing the hkl planes, (j) the interplanar distance in nm of W (110) plane and (k) The hexagonal crystal phase of WO_3 illustrated through Vesta software.

3. Results and Discussion

We fabricated the ternary CC@WO₃/GR/Au sample by a facile hydrothermal method (Fig. 1a). As shown in Fig. S1 (Supporting information), the pristine WO₃ exhibits highly oriented nanorod morphology. The crystal structure of the nanorods are purely hexagonal as depicted in Fig. 1k. Incorporating the carbon cloth fiber as a flexible electrode has led to the three dimensional growth of the ternary nanocomposite CC@WO₃/GR/Au (Fig. 1b,c). When the carbon component - graphene oxide is introduced into the metal oxide under the hydrothermal parameters, the rods are engulfed into the GO layers forming independent structures (Fig. S2, Supporting information). This paves way for the WO₃-graphene counterpart to form numerous block-like structures when embedded on the CC fiber. When the gold nanoclusters developed by the chemical reduction method (Fig. S3, Supporting information) are dispersed on the binary composite through sonication, they are decorated in the form of clusters (Fig. 1c). These cluster formations are confirmed from Fig. S4, (Supporting information) which depicts no decoration of gold before the sonication process.

The TEM image of the ternary nanocomposite of WO₃/GR/Au-nanorods is depicted in Fig. 1f which reveals the nanorods being integrated into the reduced graphene layers. The selected area electron diffraction pattern discloses the face centred cubic lattice of Au (Fig. 1e) with a respective d-spacing of 0.232 nm of the (111) plane from the HRTEM image of Fig. 1g [15]. The interplanar distance of 0.368 nm (Fig. 1j) calculated from the inverse FFT and the line intensity profile of the line drawn in the inverse FFT image (Fig. S5, Supporting information) confirms the (110) plane of the hexagonal WO₃ with respect to its SAED pattern in Fig. 1i. The EDS mapping from TEM (Fig. 1h) and the elemental compositional imaging from FESEM (Fig. 1d) confirms the presence of the elements W, C, O and Au in the respective proportions.

The particle size distribution between Au and WO₃ on the support provides clarity in understanding their interaction for hydrogen evolution reaction by affecting the surface area to volume ratio of the catalysts. Smaller particles generally have a higher surface area, leading to greater accessibility of active sites for reaction and improved catalytic activity. Additionally, the size distribution can influence the distribution of the elements within the particle, affecting the reaction kinetics to contribute to the overall performance of the catalysts in the hydrogen evolution reaction. The particle size histograms from Fig. 1c between Au and WO₃ on the support depict that the WO₃ nanorods engulfed in the graphene layers are in the size range of 3700–3900 nm, i.e. approximately nearing 4 μm (Fig. S6, Supplementary information), whereas the gold nanoparticles after reduction and the sonication process, when deposited on the binary composite of WO₃ and GR, formed cluster like formation in the size range of 110–120 nm (Fig. S6, Supplementary information). To verify, the composite of WO₃/GR/Au was also validated through TEM measurements from Fig. 1f and demonstrated in Fig. S7 a and b, Supplementary information respectively. The ternary composite reveals that the particle size distribution of WO₃ was an estimated 1.8–2 μm and that of Au was 60–65 nm respectively. The particle size of WO₃ nanorods was a decrement value when compared to that of the support as only a small portion of the composite was scanned for HRTEM analysis. To further confirm the length of the pristine nanorods, the histogram (Fig. S8, Supplementary information) from the FESEM Fig. S1 revealed that the nanorods were in the size 4–4.5 μm. The particle size from the support was roughly 0.5 μm less which is probably due to the composite formation where the nanorods were swamped into bundle-like structures with the graphene layers. Similarly, pristine gold nanoparticles from Fig. S3 revealed a particle size of 57–60 nm which correlates with the TEM results but is less than that of the Au measurements from the carbon support. This probably confirms the cluster-like formation of the gold nanoparticles after the sonication process which depicts the clusters in a higher particle distribution for aiding strong metal support interaction.

We further characterized the structural information of the HER

electrocatalysts through X-ray diffraction technology thoroughly. Fig. 2a shows three dimensional diffraction patterns of pristine WO₃, the Au decorated ternary nanocomposites of WO₃ with GO, rGO, GR and CB and the WO₃/GR/Au electrocatalyst grown on carbon fibre. All the diffraction patterns represent the hexagonal phase structure of WO₃ corresponding well with the ICDD #01–075–2187 [16]. Comparing the diffraction data of all the electrocatalysts, there is no alteration in the phase structure yet the peaks at 21.6° and 23.5° reveal an increase in broadness (Fig. 2a inset) representing the major hexagonal planes (001) and (110) of WO₃ respectively. The increase in broadness is fairly proportional to the rate of reduction of the carbon additives [17]. The prominent (001) plane of GO synthesized from the modified Hummers method and the (002) plane of the reductive rGO, GR and bulk CB reveal their amorphous nature from the individual diffraction patterns displayed in Fig. S9, (Supporting information). Regarding the CC@WO₃/GR/Au electrocatalyst, the diffraction peak at 24.4° (Fig. 2a inset) strongly resolves the carbon peak for the CC fibre (Fig. S10b, Supporting Information) which tends to be amorphous [18]. The prominent peaks of gold nanoparticles (Fig. S10a, Supporting Information) were not detected by XRD in the WO₃/GR/Au electrocatalyst as the molar percentage of gold nanoparticles was very less ~1% when compared to the binary compositions.

Raman spectroscopy conducted on the CC@WO₃/GR/Au electrode under ambient conditions confirmed the noticeable δ(O-W-O) bending and ν(O-W-O) stretching modes of WO₃ at 260 cm⁻¹ and 690 cm⁻¹ respectively (Fig. 2b). The distinguishing band of hexagonal-WO₃ (h-WO₃) is from the (001) plane of the WO₆ octahedral at 798 cm⁻¹ which in contrast is highly intense for pristine WO₃ [19]. The stretching mode of W=O at 910 cm⁻¹ is also diminished in the ternary composite which demonstrates that the introduction of carbon cloth has led to less intense band formation (Fig. S11, Supporting Information) in comparison to the powder electrocatalyst. It is noteworthy to mention that the noble metal decoration has not brought in any considerable difference in the Raman band spectra yet the respective baseline peaks of the reduced graphene layers were predominantly seen [20]. The defect-induced band (D band) and characteristic carbon-carbon bond stretching in the graphene lattice (G band) were present both for CC@WO₃/GR/Au and the WO₃/GR/Au powder sample at 1350 and 1590 cm⁻¹ respectively. The 2D band at 2700 cm⁻¹ distinguishes the reduced graphene sheets with rGO and GO indicating multiple layers involved in GR from the I_{2D}/I_G ratio [21].

As a proof of concept, to confirm the presence of gold nanoclusters and establish the oxidation state and surface compositions of the powder electrocatalysts, the surface-sensitive XPS analysis was employed. The full survey spectrum data of WO₃/GR/Au (Fig. 3a) confirms the presence of gold from the Au 4f band besides WO₃/GO/Au, WO₃/rGO/Au, and WO₃/CB/Au powders (Fig. S12, Supporting Information). The deconvolution spectra from Fig. 3a indicate that the Au 4f spectrum of WO₃/GR/Au electrocatalyst has two highly intense peaks representing the metal doublet Au 4f_{5/2} at 92.41 eV and Au 4f_{7/2} at 89.04 eV respectively. Additionally, there is also another doublet representing the oxide phase of Au 4f_{5/2} and Au 4f_{7/2} at 93.67 and 90.93 eV respectively (Fig. 3d) [22]. To understand the formation of oxide phases in Au 4f, the deconvoluted spectra of pure gold nanoparticles after the chemical reduction process revealed the absence of these oxide phases (Fig. S14, Supporting Information) indicating that the decoration of the Au nanoparticles in the form of clusters on the WO₃ and the graphene layers could be a possible reason for the oxidation through occur through sonication process. The alteration in the binding energy of the metallic response likely stems from the effect of the surrounding oxide regions of WO₃. [1]Comparing the XPS deconvoluted spectra of pristine gold nanoparticles and the Au 4f from Fig. 3d displayed in Fig. S15, Supporting Information, there is a possible shift and a peak area difference in the high intensity peaks representing the metallic phase of Au. A shift of 0.32 eV for 4f_{5/2} and 0.26 eV for 4f_{7/2} in the positive direction reveals that the phenomena of strong metal support interaction is probably

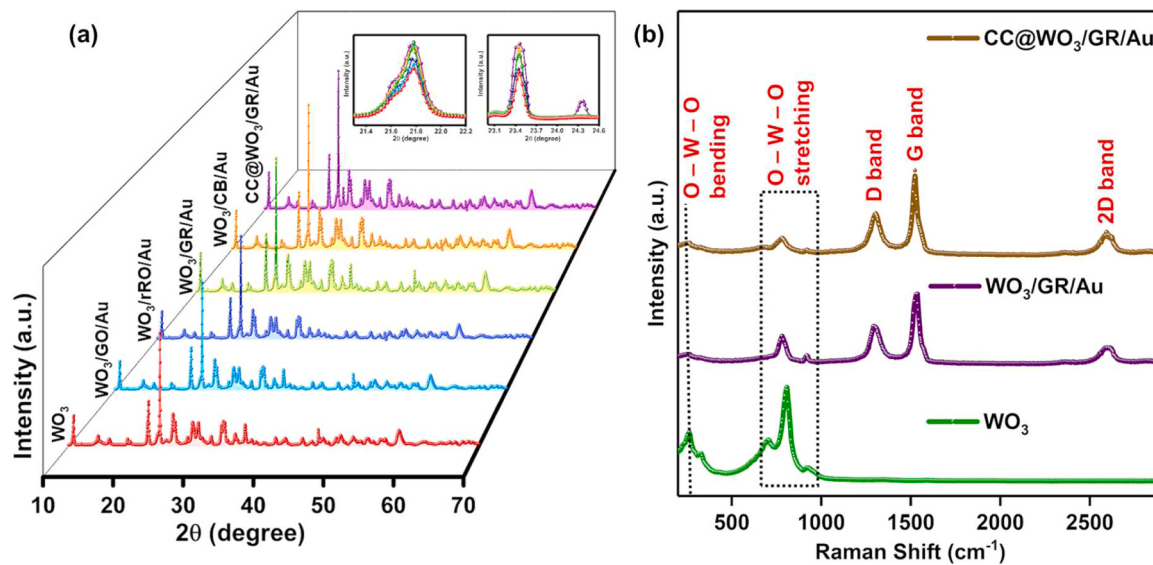


Fig. 2. (a)XRD patterns of all the electrocatalysts including $\text{WO}_3/\text{GR}/\text{Au}$ grown on carbon fiber, (b) Raman spectra of WO_3 , $\text{WO}_3/\text{GR}/\text{Au}$ and $\text{CC}@\text{WO}_3/\text{GR}/\text{Au}$.

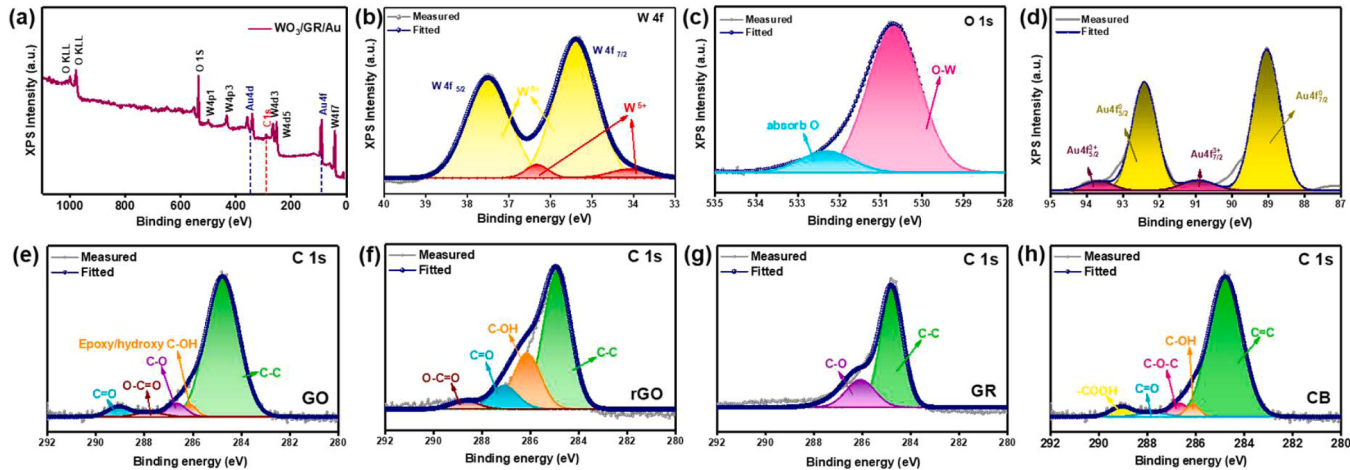


Fig. 3. (a) The XPS survey spectrum of $\text{WO}_3/\text{GR}/\text{Au}$ electrocatalysts. The high-resolution deconvoluted XPS spectra of (b) W 4 f, (c) O 1 s, and (d) Au 4 f of $\text{WO}_3/\text{GR}/\text{Au}$ electrocatalyst. The deconvoluted XPS spectra of C1s in (e) $\text{WO}_3/\text{GO}/\text{Au}$, (f) $\text{WO}_3/\text{rGO}/\text{Au}$, (g) $\text{WO}_3/\text{GR}/\text{Au}$, and (f) $\text{WO}_3/\text{CB}/\text{Au}$.

between the Au and the WO_3 -graphene layers. It is also visible that the peak area of $\text{Au 4f}_{5/2}$ and $\text{Au 4f}_{7/2}$ has decreased by 3.13% and 2.31% for the $\text{WO}_3/\text{GR}/\text{Au}$ sample. Similar findings of SMSI have been reported between Au and TiO_2 nanoparticles [2]. From the high resolution spectrum of W 4f (Fig. 3b), the spin-orbit split levels - $\text{W}4\text{f}_{7/2}$ and $\text{W}4\text{f}_{5/2}$ of W^{6+} oxidation state are revealed at 35.33 eV and 37.42 eV respectively. The low-intense peaks of $\text{W}4\text{f}_{3/2}$ portray the W^{5+} oxidation state similar to the pure WO_3 (Fig. S13, Supporting Information). The core level O 1 s spectra of $\text{WO}_3/\text{GR}/\text{Au}$ (Fig. 3c) localized at 530 eV reflect the lattice oxygen bonding with W while the peak at 532.15 eV relates to the chemisorbed oxygen species contributing to the surface groups in the carbon additives [23]. The carbon 1 s deconvoluted spectra (Fig. 3e-h) varies for all the ternary nanocomposites as the carbon species are dissimilar. The C 1 s of $\text{WO}_3/\text{GO}/\text{Au}$ generated five deconvoluted peaks located at 284.5, 286.25, 286.60, 287.72, and 289.10 eV corresponding to the C-C, epoxy/hydroxy C-OH, C-O, O-C=O, and C=O respectively. The functional groups declined as the reduction occurred yielding four bands 284.90, 286.10, 287.07 and 288.50 eV attributing to C-C, C-OH, C=O, and O-C=O respectively for the $\text{WO}_3/\text{rGO}/\text{Au}$ electrocatalyst. The core level C 1 s spectra of $\text{WO}_3/\text{GR}/\text{Au}$ were localized at two binding energies of 284.82 eV and

286.12 eV reflecting only the C-C and C-O bonds [4,24]. In contrast, the $\text{WO}_3/\text{CB}/\text{Au}$ advocated binding energies at 284.78 eV for C-C, 286.13 eV for C-OH, 286.63 eV for C-O-C, 287.81 eV for C=O, and 289.05 eV for the -COOH bond respectively [25]. Collectively, the binding energies validate the proposed ternary composite formation of all the carbon entities of WO_3 with gold decoration.

The surface area of the hybrid nanocomposite was investigated by BET and BJH (Barret-Joyner-Halenda) methods. The specific surface area of WO_3 when decorated with gold is depicted in Fig. 4c which exhibits a specific surface area of 186.25 m²/g with a pore size of 2.4 nm compared to 109.13 m²/g of pure WO_3 nanorods (Fig. S16, Supporting Information). All the samples depicted type IV isotherm with the $\text{WO}_3/\text{GR}/\text{Au}$ nanocomposite (Fig. 4d) revealing an exceptional active surface area of 250.96 m²/g with a pore size of 5.4 nm.

We comprehensively explored the electrochemical performance of the synthesized powder samples along with Pt/C for HER through systematic electrochemical procedures in acidic (0.5 M H₂SO₄) and alkaline (1 M KOH) solutions. In the 0.5 M H₂SO₄ environment, the ternary composite with reduced graphene oxide exhibited excellent catalytic performance with an overpotential of 30 mV at 10 mA cm⁻² (Fig. S17a) and a Tafel slope of 45 mV dec⁻¹ (Fig. S17b), which is comparable to the

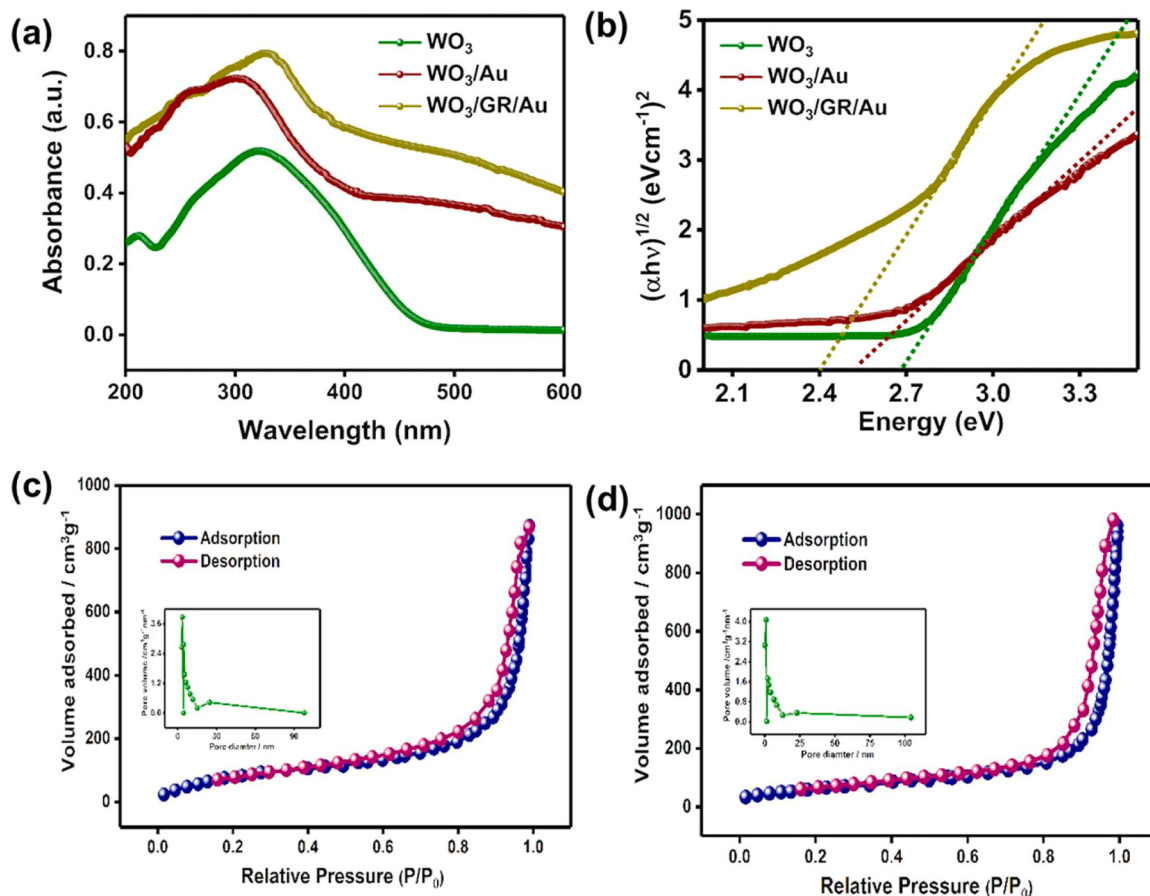


Fig. 4. (a) UV-Vis absorbance spectra and (b) Tauc's plot for WO₃, WO₃/Au and WO₃/GR/Au. Nitrogen adsorption-desorption isotherms of (c) WO₃/Au and (d) WO₃/GR/Au. Their respective BJH pore size distribution plots are displayed in the inset.

catalytic performance of Pt/C. The reason why WO₃/GR/Au exhibits high HER activity compared to the other catalysts could be attributed to the fact that the introduction of graphene layers into the WO₃ crystal structure along with the gold component could highly increase the specific area, decrease the electron-hole recombination rate to deliver efficient adsorption and mass transfer of the hydroxyl radicals favorable for hydrogen evolution reaction. [26,27] Contrastingly, the performance of the other three electrocatalysts is lower, with a Tafel slope of 56, 48, 38 mV dec⁻¹ for WO₃/rGO/Au, WO₃/GO/Au and WO₃/CB/Au respectively. Meanwhile, the WO₃/Au nanocomposite exhibited a fairer overpotential of 70 mV exhibiting a Tafel slope of 89 mV dec⁻¹. Considering the alkaline 1 M KOH solution, the efficacy is lower when compared to the acidic electrolyte (Fig. S18a, See Supporting information). This could be attributed to the stability of WO₃ in the acidic environment when compared to the basic electrolyte (Fig. 8b). [28] The Tafel slope values of all the powder electrolytes in the basic electrolyte are derived and plotted in Fig. S18b, Supporting information. From the Tafel plots, it is clear that the overpotential and Tafel slope value of WO₃/GR/Au is competent to the remarkable existing non-noble electrocatalysts (Fig. S19 and S20, Supporting Information).

To explore the practicality of the Au-decorated reduced graphene layers nanocomposite of WO₃, the powder samples were further grown on carbon cloth fiber and smeared onto stainless steel substrates to examine their HER kinetics for scalability. Under the same electrochemical conditions in the acidic and alkaline conditions, the CC@WO₃/GR/Au and SS@WO₃/GR/Au were subjected to polarization studies (Figs. 5a and 5d). Owing to the three-dimensional growth of the ternary composite in the CC substrate, the electrochemically active surface area available for the catalysis is higher than the powder catalyst being smeared onto the SS substrate. This could be attributed to the

exceptional overpotential of 20 mV at 10 mA cm⁻² and a Tafel slope of 35 mV dec⁻¹ (Fig. 5b) compared to 25 mV at 10 mA cm⁻² and 42 mV dec⁻¹ (Fig. 5e) of the SS counterpart [29]. The outcome of HER catalyzation is expectedly higher in the acidic solution revealing only satisfactory overpotential and Tafel slope values (Fig. 5d and e) of the flexible electrode and SS electrode in the basic electrolyte. The comparison of the overpotential and Tafel slope values of the electrodes are far superior to the powder catalysts coated on GCE revealing excellent concordance with the noble metal catalyst Pt/C.

Meanwhile, to understand the influence of WO₃ on the activity of HER catalysis, WO₃-free samples activity was analyzed for LSV polarization under the same conditions with and without the carbon substrate in both pH conditions. The overpotential of the GR/Au sample was 58 mV in 0.5 M H₂SO₄ solution (Fig. S21a, Supporting Information) which was comparably lesser than the WO₃/Au sample (70 mV). The Tafel slope analysis also revealed 86 mV dec⁻¹ for the substrate-free GR/Au electrocatalyst compared to 68 mV dec⁻¹ for CC@GR/Au electrode sample (Fig. S21c, Supporting Information). The results reveal that Au responsible for the initiation of the SMSI effect delivers massive catalytic outcomes with the graphene layers when compared to the WO₃ oxide. As expected, the conclusion in the basic electrolyte medium (Fig. S21b and d) was lesser than the acidic counterpart. The electrochemical behavior of WO₃ and WO₃/GR/Au catalysts was studied using cyclic voltammetry in 0.5 M H₂SO₄ solution to understand the catalytic active sites and structure evolution. The CV curves of WO₃ and WO₃/GR/Au showed different redox peaks, with the redox peaks between 0.3 and 0 V for WO₃ assigned to H⁺ insertion and removal in WO₃ leading to the formation of tungsten bronze (Fig. S22a, Supplementary Information). On the contrary, the significant increase of current in the potential range between 0.35 and 0.1 V for the WO₃/GR/Au electrocatalyst is due to specific

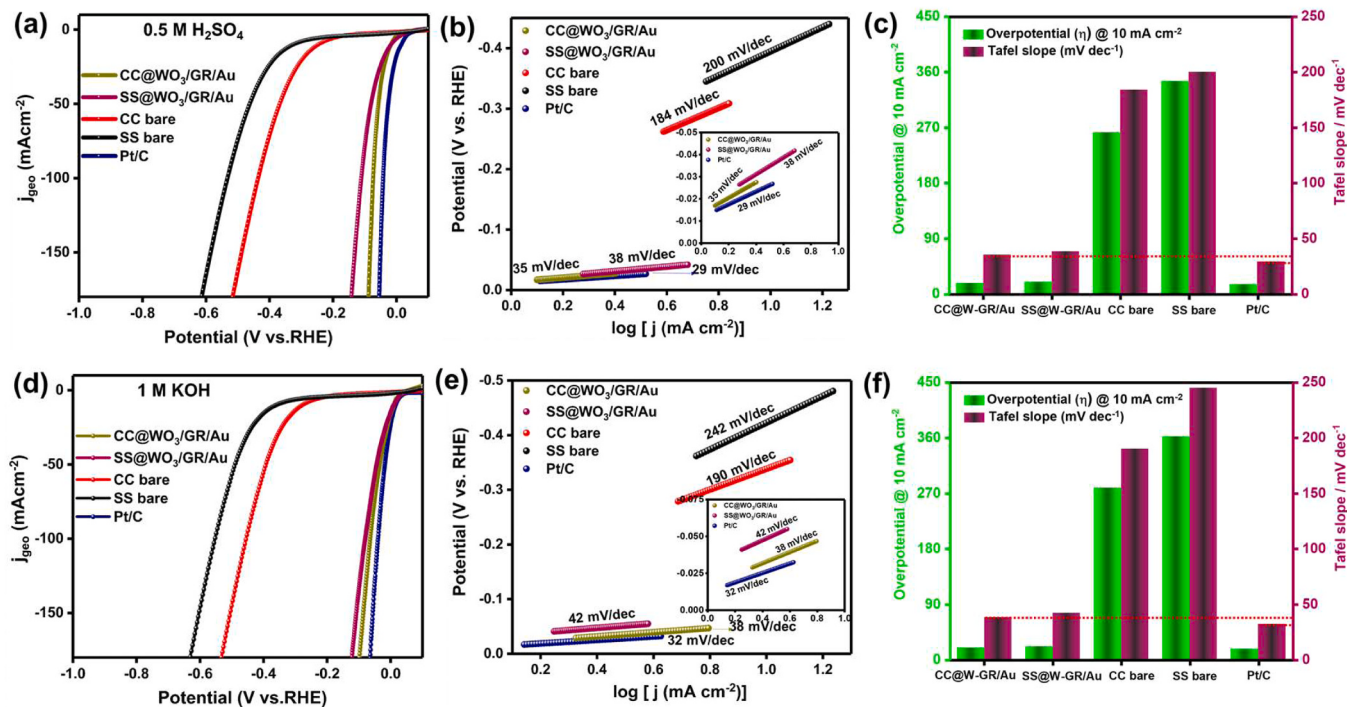


Fig. 5. The LSV polarization curves recorded for SS bare, CC bare, SS@WO₃/GR/Au electrode, and CC@WO₃/GR/Au electrode in (a) acidic and (d) alkaline electrolytes respectively. The Tafel slope analysis of SS bare, CC bare, SS@WO₃/GR/Au electrode, and CC@WO₃/GR/Au electrode at (b) pH = 0 and (e) pH = 14 respectively. The comparison of $\eta_{@10 \text{ mA cm}^{-2}}$ vs Tafel slope for SS bare, CC bare, SS@WO₃/GR/Au electrode, and CC@WO₃/GR/Au electrode in extreme (c) acidic and (f) basic electrolytes respectively.

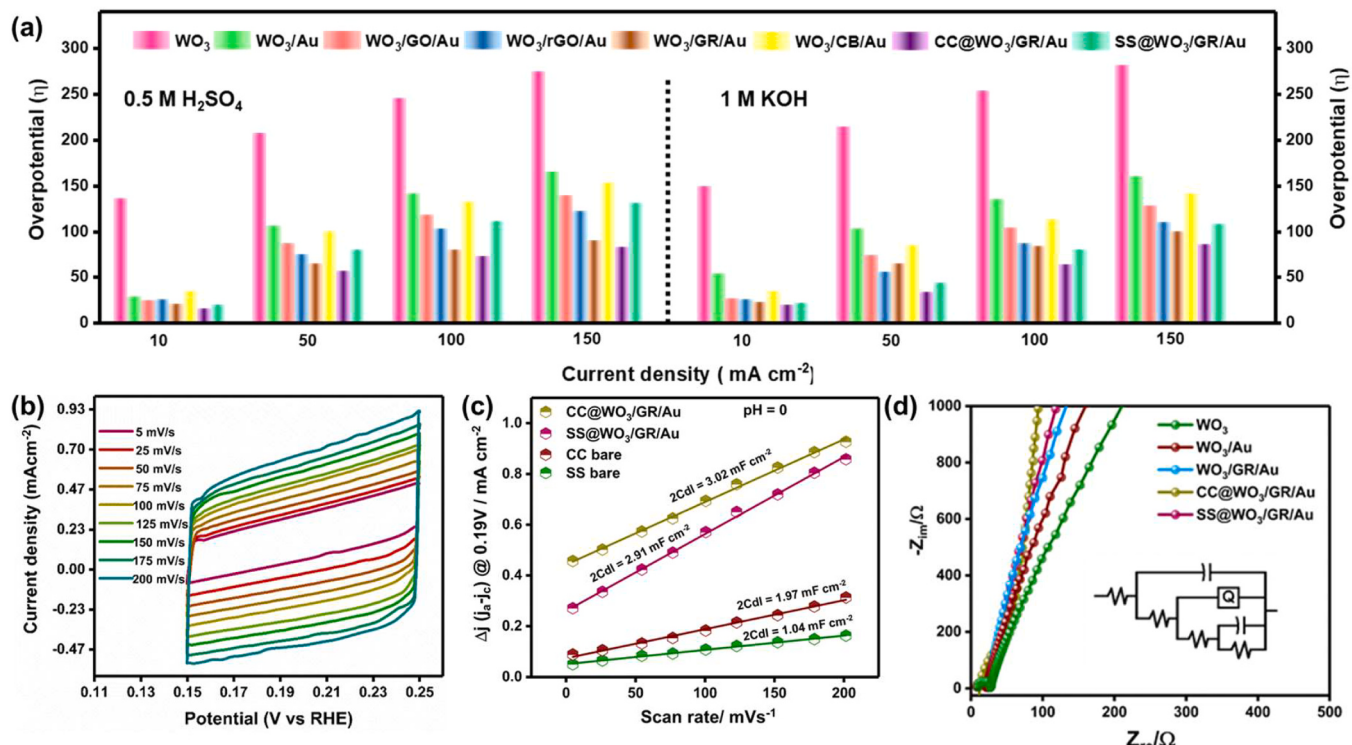


Fig. 6. (a) The comparison of the overpotential values at different current densities of all the electrocatalysts in acidic and basic solutions, (b) The cyclic voltammetry curves in the non-faradaic region of the CC@WO₃/GR/Au in the acidic (0.5 M H₂SO₄) electrolyte, (c) The capacitance obtained from the fit of double-layer charging current density versus scan rate for CC@WO₃/GR/Au and SS@WO₃/GR in the acidic electrolyte, (d) The Nyquist plot of all the electrocatalyst powders with the equivalent circuit diagram in the inset.

hydrogen adsorption on Au ions (Fig. S22b, Supplementary Information). The positive shift of the reduction peak at around 0.25 V makes the H^+ insertion/out process more reversible due to the presence of graphene layers. It is also visible that the redox potential range is higher for the $WO_3/GR/Au$ electrocatalyst compared to the pure WO_3 electrocatalyst. At lower potentials (0.1–0.01 V), the formation of hydrogen adsorption intermediates results in an increase in current compared to pristine WO_3 , indicating that Au atoms in the $WO_3/GR/Au$ electrocatalyst are the active sites for the commencement of hydrogen evolution reaction (HER).

To investigate the catalytic performance of the electrocatalysts deeper, the electrical double layer capacitance (C_{dl}) and the electrochemical impedance spectroscopy were plotted for the electrode samples of $WO_3/GR/Au$. The capacitance curves from the non-faradaic region at different scanning speeds for CC@ $WO_3/GR/Au$ and SS@ $WO_3/GR/Au$ in the acidic electrolyte are shown in Fig. 6b and Fig. S23 (Supporting Information) respectively. The electrical double layer capacitance value is derived from the calculation (see supporting information) and the fitting performed on the CV data at a potential of 0.19 V. As shown in Fig. 6c, the CC electrode possesses the highest C_{dl} value of 3.02 mF cm^{-2} compared to the C_{dl} value of SS, 2.91 mF cm^{-2} . The C_{dl} values of the same electrodes were swept in the basic electrolyte (Fig. S24, Supporting Information), and the observations led to a slight decrease in the C_{dl} values depicting that the adsorption of the H^+ species is better in the acidic environment compared to the OH^- ions in the alkaline electrolyte.

3.1. HER kinetic differences in acid and alkaline conditions

Unraveling the kinetics involved in H_2 production is essential to understand the thermodynamical pathways in which the electrocatalysts work with the electrolyte media to process the hydrogen evolution reaction. The combination of two protons to produce a diatomic hydrogen gas molecule from the electrode surface is a multistep approach that includes adsorption, reduction, and desorption of the adsorbed species. The initiation of the HER mechanism includes three pathways - Volmer, Heyrovsky, or the Tafel pathways, any two of which are adopted by any electrocatalyst to initiate the catalytic process. These pathways/mechanisms are solely dependent on the external electrolyte

medium and the catalytic effectiveness of the electrocatalyst taken. In the 0.5 M H_2SO_4 electrolyte, the primary intermediate is a proton source developed from the hydronium cation during the protonation of water. This adsorbed proton combines with an electron from the active surface of the electrode to develop into H_{ads} referred to as the Volmer reaction. The probability of the adsorbed hydrogen combining with another H_{ads} leads to the Volmer - Tafel pathway which otherwise would couple with another proton from the Arrhenius acid molecule to evolve H_2 gas known as the Volmer - Heyrovsky pathway. In the 1 M KOH electrolyte, the hydroxide ion initiates the Volmer process by interacting with an adsorbed hydrogen species released from the electrode active surface. The adsorbed hydrogen species combine with another electron from H_2O to release hydrogen gas molecules. On the contrary, the Tafel mechanism is likely to occur when two such adsorbed hydrogen atoms combine to evolve hydrogen gas. The ΔGH^* value of the electrocatalyst determines the reaction pathways where a positive ΔGH^* hinders the Heyrovsky or Tafel steps and a negative ΔGH^* favors the Volmer reaction. Therefore, an optimal ΔGH^* should be nearing zero for an active catalyst. [30,31] One could also deduce the pathways approximately depending on the Tafel slope values obtained. The predominance of the Volmer pathway is realized when the Tafel slope is around 120 mV/dec , $\sim 40 \text{ mV/dec}$ signifies the Heyrovsky step, and $\sim 30 \text{ mV/dec}$ indicates that the respective electrocatalyst has gone through the Tafel pathway. [32] In distinction to these mechanistic pathways of HER, we could infer that all the synthesized electrocatalysts of WO_3 screened for HER catalysis in the electrochemical setup (Fig. 7b) follows Volmer - Heyrovsky mechanism with the CC@ $WO_3/GR/Au$ and SS@ $WO_3/GR/Au$ electrocatalyst bordering near the Tafel mechanism. The noble metal catalyst Pt/C trails the Volmer – Tafel mechanism and henceforth owns the least Tafel slope.

3.2. Bifunctional effect of strong metal support interaction (SMSI) and hydrogen spillover effect (HSPE) for Hydrogen evolution reaction

The pronounced HER performance of the hybrid WO_3 electrocatalyst could be attributed to the bifunctional effect of both strong metal support interaction (SMSI) and hydrogen spillover effect (HSPE). The SMSI is an interfacial phenomenon that focuses on the thermodynamical kinetics required for the initial catalysis of HER at the metal support

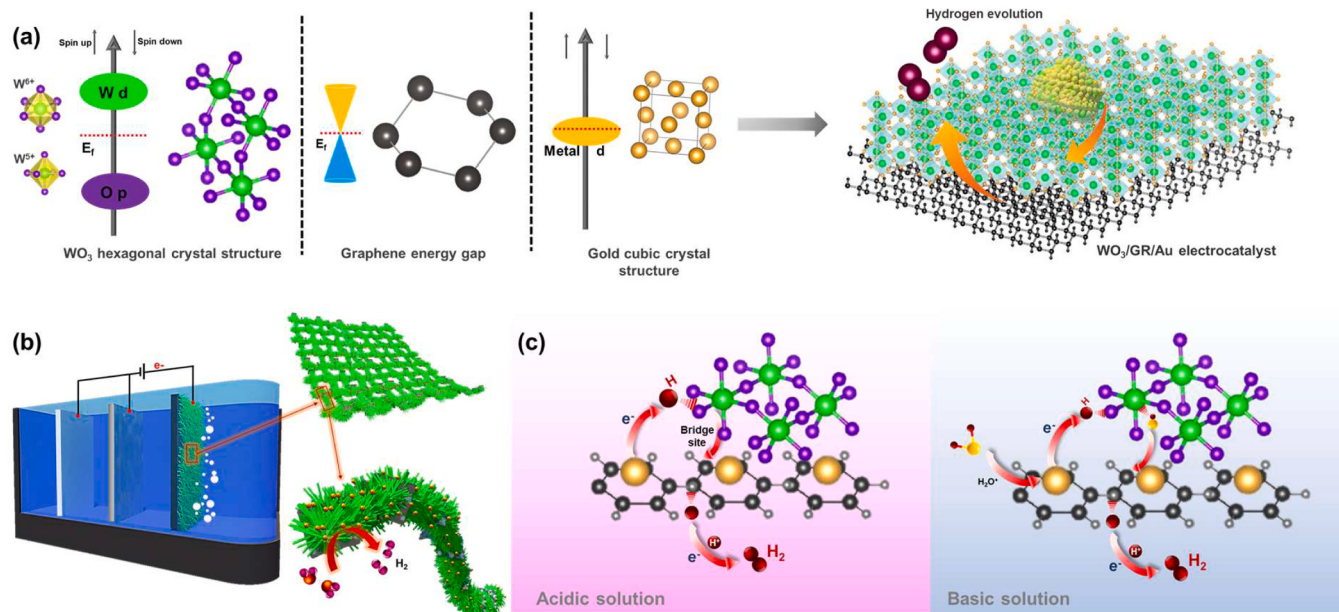


Fig. 7. Schematic representation of (a) the electronic states of WO_3 , graphene, and gold metal leading to the formation of the three-dimensional electrocatalyst $WO_3/GR/Au$ exhibiting SMSI, (b) three-electrode set up of CC@ $WO_3/GR/Au$ electrode for hydrogen evolution reaction, (c) the bifunctional effect of SMSI and HSPE of the electrocatalyst electrode for hydrogen evolution reaction.

interface.^[6,13] In contrast, the HSPE occurs when the adsorbed/desorbed species attains a threshold to migrate from the metal surface to another catalytic support site to deliver hydrogen gas molecules.^[33,34] In our study, the strong metal support interaction takes place at the perimeter of the decorated gold nanoclusters and the metal oxide WO_3 forming dual reaction sites. The interfacial phenomena besides involving chemical reactions also trigger charge redistribution between the metal-support interface. The population of gold nanoclusters at the interface of the WO_3 nanorods (Fig. S25, Supporting Information) and the carbon species are responsible for the initiation of the adsorption process. The Au nanoclusters with high charge density transfer the electrons from the Au 4 f orbital to the surface of WO_3 , similar to the previously reported observations.^[35,36]

The confirmation of SMSI could also be established from the negative shift in the Au 4 f binding energies (Fig. 3d) signifying charge transfer from Au to W atom along with the modifications in the electronic structure of Au. The charge transition occurs between the interatomic orbitals of Au5d and either the O2p or the W5d orbitals (Scheme 7a). This leads to the molecular energy level shift due to the orbital rehybridization in the metal-support interface which lowers the energy barrier and reinforces the adsorption intermediates facilitating the dynamics of HER catalysis.^[6,13,36] The electron density redistribution between the noble metal and the metal oxide leads to SMSI with appropriate changes in the oxidation state of the noble metal Au (Scheme 7a). In the reacting electrolyte, the electron transfer creates metal-support bonds where the electron cloud is high leading to a decrease in the bandgap thereby strengthening the SMSI.^[5,36] This could be linked to the least bandgap (Fig. 4b) for the $\text{WO}_3/\text{GR}/\text{Au}$ electrocatalyst, 2.4 eV compared to 2.7 eV for pristine WO_3 calculated from the absorption spectra (Fig. 4a). In the acidic environment, the reduction in the valence state of Au accelerates the hydrogen adsorption process, whereas, in the alkaline environment, the oxidation state increases to promote water dissociation through the release of a CO molecule. Nevertheless, an optimal valence state of Au (+3) is advantageous for optimal H^* and OH^* adsorption.^[37]

Subsequently, following the strong metal support interaction, the absorbed species migrate from the WO_3 interface onto the carbon support through the process of Hydrogen spillover effect (HSPE). For the HSPE to commence and evolve hydrogen gas, two main counterparts are essential - a surface (usually metal) capable of absorbing the dissociated hydrogen species from the donor/electrolyte and secondly an acceptor (usually carbon support) which acts as a receiver of the hydrogen species through which hydrogen spillover proceeds. In our present work, W atoms act as the metal component and the reduced graphene layers which surpassed other carbon entities showcasing outstanding conducting nature serve the purpose of an acceptor.^[4,38] Owing to the strong sp^2 hybridization over the sp^3 hybridized carbon atoms, strong π - π interactions dominate the carbon framework in the graphene oxide constituent of $\text{WO}_3/\text{GR}/\text{Au}$ electrocatalyst.^[39] The HSPE reaction pathway in the $\text{WO}_3/\text{GR}/\text{Au}$ electrocatalyst includes the proton adsorption by the WO_3 surface as a result of the SMSI effect from the Au nanoclusters followed by the migration of the proton towards the carbon support where the final H_2 desorption takes place.^[5,40,41] The Gibbs free energy (ΔG_{H^*}) is also an essential parameter that evaluates the rate of the HER reaction although the mechanisms are pronounced for the Hydrogen evolution reaction to occur. A ΔG_{H^*} with a negative value favors the Vomer reaction and a vast positive ΔG_{H^*} hinders the rate-determining Heyrovsky or Tafel steps. Therefore the Gibbs free energy should be negative and approaching near zero for an optimum electrocatalyst. In our case, the $\Delta G_{\text{H-metal}} < 0$ for the tungsten metal and the defective reduced graphene sheets have a $\Delta G_{\text{H-support}} > 0$ which supports the interfacial hydrogen migration. As a result, a Schottky junction is created to initiate the interfacial charge flow between the interface of the metal surface and the support.^[42] Integrating both the respective energies could stimulate the H^+ adsorption and H_2 desorption kinetically thereby eliminating the use of Pt-based electrocatalysts yet

delivering exceptional HER performance.

The interaction between the different adsorptive species determines the rate of the HSPE mechanism. The H^+ adsorption in the acidic medium and the OH^- adsorption in the alkaline medium are the kick-off terminals for the hydrogen spillover mechanism. In the acidic environment, a bridge site is developed between the W-O interface and the defective graphene support which favors the migration of the H species from the W-O interface to the reduced graphene layers developing a transitory chemical bond with the surficial carbon atoms.^[43] In the case of the basic Ph, the adsorption occurs at two reaction sites the W (OH^-) and O (H^+) which is probably why the HER kinetics delays when compared to the acidic counterpart. Eventually, this could be the possible reason for the lower overpotential and Tafel slope values of the binary carbon-based WO_3 electrocatalysts in the acidic medium compared to the alkaline environment. The final desorption of the adsorbed hydrogen atoms through the spillover mechanism occurs via C-H bond formations to assist in the evolution of hydrogen gas molecules. The number of C-H bond formations also depends on the conductivity of the carbon support surface.^[44,45] which is likely a possible explanation for why the reduced graphene sheets outperformed the GO, rGO, and bulk CB counterparts in the rate kinetics of HER with WO_3 . The schematic rendering of the mechanism of SMSI and HSPE of the $\text{WO}_3/\text{GR}/\text{Au}$ electrocatalyst electrode for hydrogen evolution reaction is represented in Fig. 7c.

3.3. Stability profile through Pourbaix profiles

The reaction kinetics in the acidic pH has outperformed those in the basic pH as is visible from Fig. 6a where the overpotential values of all the electrocatalysts at different current densities are lower in the acidic electrolyte medium. To identify why WO_3 performs well in the acidic medium and to understand the intermediates involved during the HER electro kinetics and their stability influence on the pH spectrum, 2D and 3D Pourbaix diagram was employed.^[28]

The E-pH plot of water dissociating into oxygen and hydrogen at their respective potentials is depicted in Fig. 4d governed by the Nernst equation. Similarly, the stability of tungsten in a broad pH spectrum taking into consideration the pH, concentration of the W species, and the applied potential (V) was employed to construct a 3D stability profile (Fig. 8b) of W. To understand the reaction kinetics and to draw attention to the corrosive properties for long cyclic tests, the concentration of the soluble species of W, C, and Au taken for the study were 1×10^{-8} mol/kg at 298 K. In Fig. S26, Supporting Information, the essential information demonstrating the stability of WO_3 in terms of the E-pH plot with the concentration at 1×10^{-8} mol/kg of the soluble species is displayed. As seen in the figure, the location of the stability limits for the WO_3 falls in the lower pH region, while the tungstate ions (WO_4^{2-}) and the polytungstate ion ($\text{HW}_6\text{O}_{21}^{5-}$) species dominate the neutral and alkaline pH values respectively. The reflection of tungsten's Pourbaix stability shows that it is corrosion resistant when the potential is adjusted below $Eh = -1.2$ V suggesting that the capacity of WO_3 under acidic circumstances is stable enough to evolve hydrogen gas molecules below the specified voltage.^[46] Carbon's Pourbaix diagram from Fig. S27 (Supporting Information) suggests that it is thermodynamically unstable over the alkaline range of pH due to its inherent corrosion potential. To favor the hydrogen evolution reaction, the H^+ ions should be absorbed, as protonation is necessary to maintain the equilibrium potential as well as to catalyze HER in acidic circumstances. Carbon requires four electrons (oxidation state of +4) to result in an oxide that is hindered in acidic conditions by high activation energy barriers.^[12,45]

An increase in HER activity was associated with an excess of protons at low pH levels. Nevertheless, the alkaline environment requires the formation of OH^- ions rather than the consumption of H^+ ions. Considering both cases, water functions as a proton donor for the latter. The standard electrode potentials regarding the carbon are specified in Table S1, Supporting Information. Combining both the states of W and C

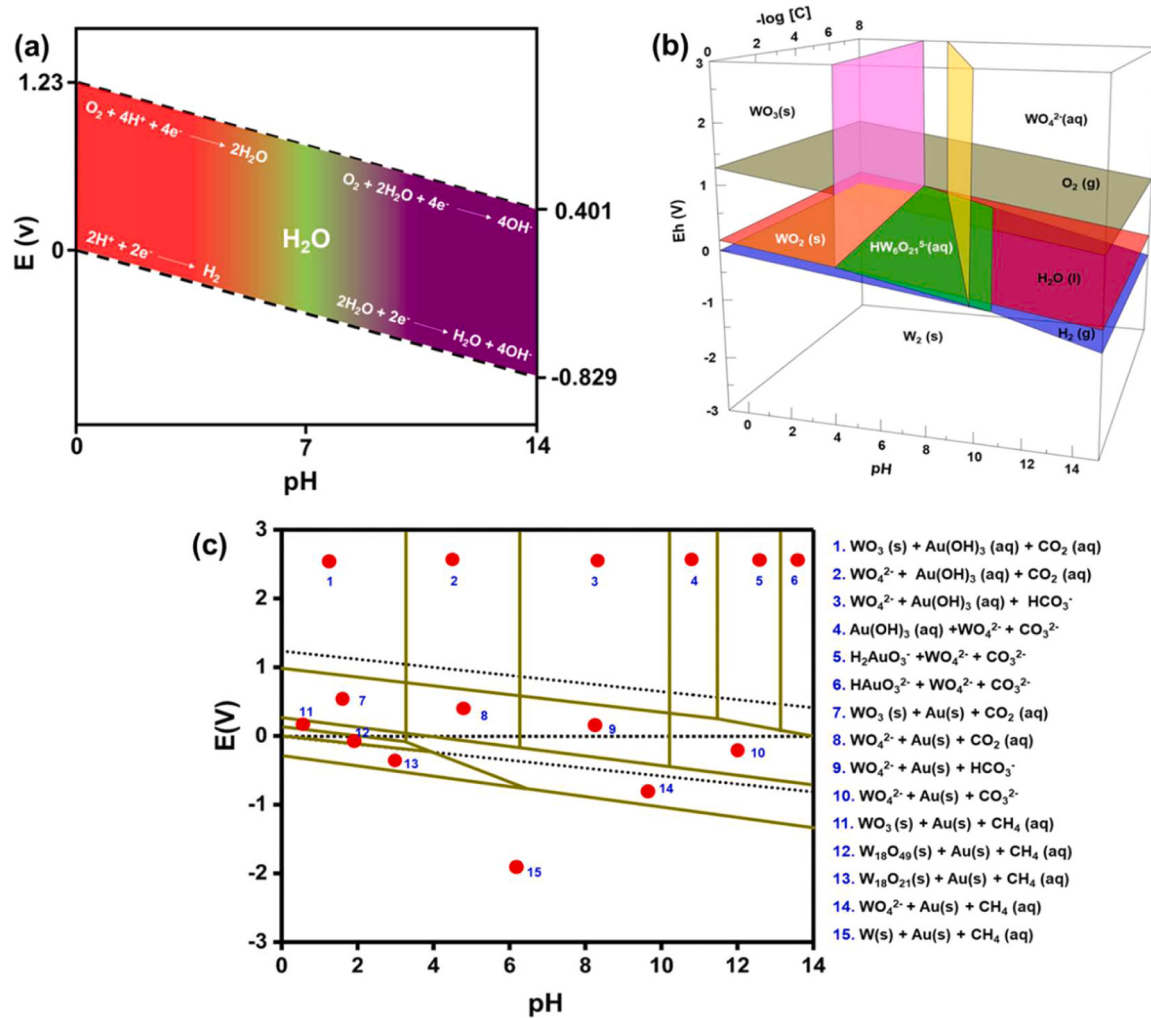


Fig. 8. The Pourbaix stability profile of (a) water, (b) tungsten - 3D E-pH-C plot and (c) The E-pH stability plot of W, C, and Au.

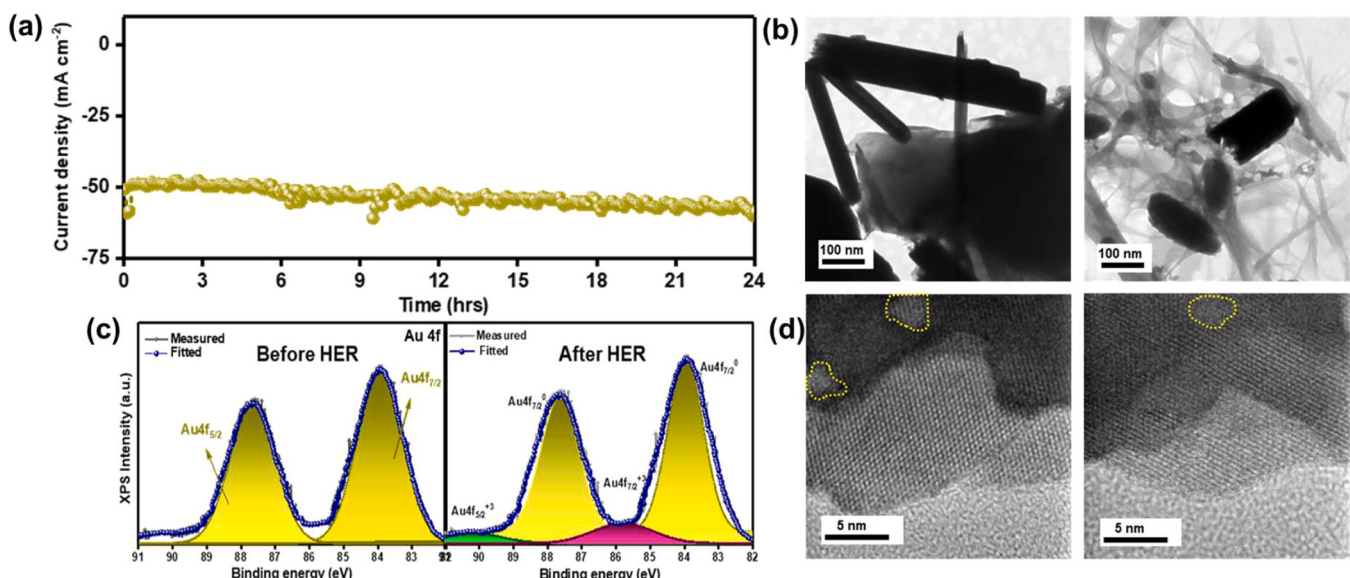


Fig. 9. (a) The long cycle stability test of the CC@WO₃/GR/Au in the acidic (0.5 M H₂SO₄) electrolyte, (b) the before and after TEM images of the same catalyst, (c) The XPS analysis of Au 4 f deconvoluted spectra after the stability test, and (d) The HR-TEM image of gold nanoclusters observed for SMSI during HER of the electrocatalyst CC@WO₃/GR/Au and the diminishment of gold nanoclusters observed after HER in the HR-TEM image.

in the ratio 8:2, the reaction intermediates are illustrated in Fig. S28 and Table S2, Supporting Information. The stable kinetics of Au in the vast pH spectra (Fig. S29, Supporting Information) signifies the excellent stability of the material to be used in high-end catalysis. Merging the three elements which are necessary for the formation of the nanohybrids $\text{WO}_3/\text{GR}/\text{Au}$, the stability plot is depicted in Fig. 4f with its reaction intermediates. The results prove the strength of the electrocatalyst is strong in the acidic media with intermediates such as $\text{WO}_3(\text{s}) + \text{Au}(\text{s}) + \text{CO}_2(\text{aq})$ in the acidic pH range. These stability results are also proof that the hydrogen evolution outcomes are more effective in the acidic media when compared to the basic counterpart revealing slightly slower kinetics [26, 47, 48].

To evaluate the HER stability of the $\text{CC@WO}_3/\text{GR}/\text{Au}$ electrode for scalable applications, the chronoamperometric measurements were performed sequentially for over 24 h in a high-concentration acidic solution (0.5 M H_2SO_4). As depicted in Fig. 9a, the current density is stable with few disruptions for a period of 24 h [21].

Furthermore, the electrocatalyst was screened for XPS and HR-TEM after the chronoamperometric assessment and the $\text{CC@WO}_3/\text{GR}/\text{Au}$ electrode exhibited satisfactory structural stability with the graphene layers utilized to its maximum efficiency (Fig. 9b) indicating that the catalyst has undergone oxidation. The deconvoluted Au 4 f spectra of the $\text{CC@WO}_3/\text{GR}/\text{Au}$ showed a higher level of oxidized doublet compared to the $\text{WO}_3/\text{GR}/\text{Au}$ powder electrocatalyst (Fig. 5d). This could be due to the introduction of the carbon cloth fiber during the hydrothermal process and the thermal nucleation process which might have heightened the oxidation in Au. It also focuses on the increasing SMSI interaction (Fig. 9c) between the oxide and the graphene support layers which could aid in the enhancement of the HER activity. The before and after Au 4 f do not show major changes in the peak positions of the Au 4 $f_{5/2}$ and 4 $f_{7/2}$ metallic doublet binding energies (92.47 and 89.16 eV respectively) (Table S4, Supplementary Information). But in the case of the oxide doublet, comparing the binding energies, the area of the deconvoluted peak shows a wide difference of 16% increment in the Au 4 $f_{5/2}^{3+}$ oxidation state revealing the $\text{CC@WO}_3/\text{GR}/\text{Au}$ electrode has undergone oxidation after the 24-hour long term stability test. On the contrary, the area of Au 4 $f_{7/2}^{3+}$ after HER catalysis increased only by 0.94%. From the above-briefed explanation, it is clear that $\text{CC@WO}_3/\text{GR}/\text{Au}$ electrocatalyst has undergone some level of oxidation. The LSV polarization curves scanned after the long-term stability tests (Fig. S32, Supporting Information) revealed an increase in the overpotential value of 12 mV at 50 mA cm⁻². The FESEM image after the long-term assessment also proves that the WO_3 nanorods along with the graphene and Au clusters were utilized to the maximum and displayed a reduction in the nanorod length (Fig. S33, Supporting Information). When a portion of the electrocatalyst was scanned for HR-TEM analysis (Fig. 9d) after the stability test, results expose the gold nanoclusters and the outer layers of the WO_3 oxide a little worn yet with an intact interplanar distance indicating good adherence of the electrocatalyst onto the substrate even after long hours of electrochemical tests. [7, 43, 49] The EDX analysis reveals the change in the composition of the W, C, O, and Au elements (Fig. S34, Supporting Information) before and after the HER endurance test. The before and after elemental analysis of the fresh and spent samples indicate that the spent sample has been oxidized to a smaller extent which is visible with the difference in the atomic weight percentage values. Also, the addition of gold precursor was 1 wt %, but the results from the weight percentage of the fresh sample show 1.2%. This could be attributed to the sputtering of gold nanoparticles before vacuuming the sample for the FESEM and EDAX analysis. There has been a reduction in the Au elemental composition too which implies that the Au nanoparticles have been effectively involved in the catalytic reaction for hydrogen evolution reaction.

The catalytic site for the hydrogen evolution reaction (HER) in WO_3 is typically the surface oxygen atoms (O site). WO_3 has been found to bind to Au nanoparticles via strong chemical interactions also known as the strong metal support interaction (SMSI) between the surface oxygen

atoms of WO_3 and the Au atoms evident from Fig. S15, Supporting Information. This is because the oxygen atoms are highly electronegative, meaning they have a strong tendency to attract electrons which allows the oxygen atoms to form strong chemical bonds with the Au atoms. In the case of binding between WO_3 and graphene layers, it is also typically the surface oxygen atoms of WO_3 that bind to the carbon atoms in the graphene. Hence as proposed in the mechanism of hydrogen evolution reaction in the hybrid electrocatalyst, the adsorption of hydrogen molecules typically takes place on the surface of the Au and WO_3 catalysts and thereby transferring the adsorbed species to the carbon support of reduced graphene layers for the desorption/evolution of H_2 gas molecules. Practically, the active sites for the hydrogen evolution reaction for the individual electrocatalyst $\text{WO}_3/\text{GR}/\text{Au}$ coated on two different substrates carbon cloth (CC) and stainless steel (SS) substrates, and in different pH media were identified by integrating the total charge through the cyclic voltammetry method. The CV measurements were run in the potential range of $-0.2\text{--}0.6$ V vs. RHE for all the samples and the upper limit of the active sites was determined using the equation $n = Q / 2 F$. [3] Here Q is the whole charge of the CV curve derived by integrating the area of the curve (anodic and cathodic voltammetric charges) and represented in Fig. S31 (a-d), Supporting Information. The number of active sites of the electrocatalysts is tabulated in Table S3 with the $\text{CC@WO}_3/\text{GR}/\text{Au}$ electrocatalyst representing the largest number of active sites with 1.172×10^{-5} mol in the acidic medium. The fabricated $\text{CC@WO}_3/\text{GR}/\text{Au}$ and $\text{SS@WO}_3/\text{GR}/\text{Au}$ electrodes work exemplarily when compared to the previously reported WO_3 -based catalysts for their HER kinetics. The full cell results using $\text{CC@WO}_3/\text{GR}/\text{Au}$ electrode for HER and $\text{CC@Ru}_2\text{O}$ for OER are depicted through LSV polarization results and displayed in Fig. S30 displaying an overall cell voltage of 1.56 V at 10 mA cm⁻². The comparison is concluded with the Tafel slope and overpotential ($\eta_{@10}$) values of all the electrocatalysts depicted in Fig. S35, Supporting Information. The aforementioned results emphasize that the compositional engineering strategy of the ternary hybrid electrocatalysts in our work provides an avenue to understand the kinetics behind HER through SMSI and HSPE thereby enhancing the performance of HER catalysis in a wide pH range.

4. Conclusion

In summary, we have made a thorough investigation of the catalysis strategy of HER in the Au decorated WO_3 supported on reduced graphene layers by SMSI and HSPE effect. The developed three-dimensional flexible electrode delivers exceptional HER performance of 26 and 34 mV at a current density of 10 mA cm⁻² and a striking Tafel slope of 39 and 42 mV dec⁻¹ in acidic and basic electrolyte environments respectively. A current density of 10 mA cm⁻² was achieved by the $\text{CC@WO}_3/\text{GR}$ electrode ensuring excellent durability and a stable potentiostatic profile for extended hours of practicality. This superior performance could be attributed to the intrinsic activity between the multifunctional active sites of the electrocatalyst via the strong metal interaction between the gold nanoclusters and the WO_3 matrix and the excellent migration capability of the adsorbed species through the hydrogen spillover effect on a conductive graphene matrix. Unraveling the kinetics behind the stability of $\text{CC@WO}_3/\text{GR}/\text{Au}$ opens new avenues for scaling the 3D hybrid electrocatalyst for efficient hydrogen production.

CRediT authorship contribution statement

R. Rajalakshmi: Conceptualization, Methodology, Investigation, Writing - original draft, Writing - review & editing. **G. Srividhya:** Formal analysis, Writing - original draft. **C. Viswanathan:** Formal analysis. **N. Ponpandian:** Resources, Supervision, Project administration.

Declaration of Competing Interest

The authors declare that they have no known competing financial interests or personal relationships that could have appeared to influence the work reported in this paper.

Data Availability

Data will be made available on request.

Acknowledgments

The authors thank the DST-SERB for the funding [EMR/2016/007676] as well as the DST-FIST, DST-PURSE, UGC-SAP, Government of India for the support of instrumental facilities available in the department. The authors would like to acknowledge the XPS facility from SRM University, Chennai.

Appendix A. Supporting information

Supplementary data associated with this article can be found in the online version at [doi:10.1016/j.apcatb.2023.123089](https://doi.org/10.1016/j.apcatb.2023.123089).

References

- [1] J.A. Turner, Sustainable hydrogen production, *Science* 305 (2004) (1979) 972–974, <https://doi.org/10.1126/science.1103197>.
- [2] D.E.H.J. Gernaat, H.S. de Boer, V. Daioglou, S.G. Yalem, C. Müller, D.P. van Vuuren, Climate change impacts on renewable energy supply, *Nat. Clim. Change* 11 (2021) 119–125, <https://doi.org/10.1038/s41558-020-00949-9>.
- [3] J. Li, J. Hu, M. Zhang, W. Gou, S. Zhang, Z. Chen, Y. Qu, Y. Ma, A fundamental viewpoint on the hydrogen spillover phenomenon of electrocatalytic hydrogen evolution, *Nat. Commun.* 12 (2021) 3502, <https://doi.org/10.1038/s41467-021-23750-4>.
- [4] A.C. Ghogia, S. Cayez, B.F. Machado, A. Nzihou, P. Serp, K. Soulantica, D. Pham Minh, Hydrogen spillover in the fischer-tropsch synthesis on carbon-supported cobalt catalysts, *ChemCatChem* 12 (2020) 1117–1128, <https://doi.org/10.1002/cctc.201901934>.
- [5] P. Wu, S. Tan, J. Moon, Z. Yan, V. Fung, N. Li, S.-Z. Yang, Y. Cheng, C.W. Abney, Z. Wu, A. Savara, A.M. Momen, D. Jiang, D. Su, H. Li, W. Zhu, S. Dai, H. Zhu, Harnessing strong metal–support interactions via a reverse route, *Nat. Commun.* 11 (2020) 3042, <https://doi.org/10.1038/s41467-020-16674-y>.
- [6] Y. Zhang, J.-X. Liu, K. Qian, A. Jia, D. Li, L. Shi, J. Hu, J. Zhu, W. Huang, Structure sensitivity of Au-TiO₂ strong metal–support interactions, *Angew. Chem. Int. Ed.* 60 (2021) 12074–12081, <https://doi.org/10.1002/anie.202101928>.
- [7] X. Zou, Y. Zhang, Noble metal-free hydrogen evolution catalysts for water splitting, *Chem. Soc. Rev.* 44 (2015) 5148–5180, <https://doi.org/10.1039/C4CS00448E>.
- [8] Y. Zhu, Q. Lin, Y. Zhong, H.A. Tahini, Z. Shao, H. Wang, Metal oxide-based materials as an emerging family of hydrogen evolution electrocatalysts, *Energy Environ. Sci.* 13 (2020) 3361–3392, <https://doi.org/10.1039/D0EE02485F>.
- [9] G. Mineo, M. Scuderi, E. Bruno, S. Mirabella, Engineering hexagonal/monoclinic WO₃ phase junctions for improved electrochemical hydrogen evolution reaction, *ACS Appl. Energy Mater.* 5 (2022) 9702–9710, <https://doi.org/10.1021/acsaem.2c01383>.
- [10] Q. Liu, F. Wang, H. Lin, Y. Xie, N. Tong, J. Lin, X. Zhang, Z. Zhang, X. Wang, Surface oxygen vacancy and defect engineering of WO₃ for improved visible light photocatalytic performance, *Catal. Sci. Technol.* 8 (2018) 4399–4406, <https://doi.org/10.1039/C8CY00994E>.
- [11] X. Wang, L. Pang, X. Hu, N. Han, Fabrication of ion doped WO₃ photocatalysts through bulk and surface doping, *J. Environ. Sci.* 35 (2015) 76–82, <https://doi.org/10.1016/j.jes.2015.04.007>.
- [12] Y.K. Recepoglu, A.Y. Goren, Y. Orooji, A. Khataee, Carbonaceous materials for removal and recovery of phosphate species: Limitations, successes and future improvement, *Chemosphere* 287 (2022), 132177, <https://doi.org/10.1016/j.chemosphere.2021.132177>.
- [13] W.T. Figueiredo, G.B. dellaMea, M. Segala, D.L. Baptista, C. Escudero, V. Pérez-Dieste, F. Bernardi, Understanding the strong metal–support interaction (SMSI) effect in Cu_xNi_{1-x}/CeO₂ (0 < x < 1) nanoparticles for enhanced catalysis, *ACS Appl. Nano Mater.* 2 (2019) 2559–2573, <https://doi.org/10.1021/acsamm.9b00569>.
- [14] H. Yu, B. Zhang, C. Bulin, R. Li, R. Xing, High-efficient synthesis of graphene oxide based on improved hummers method, *Sci. Rep.* 6 (2016) 36143, <https://doi.org/10.1038/srep36143>.
- [15] G. Geng, P. Chen, B. Guan, Y. Liu, C. Yang, N. Wang, M. Liu, Sheetlike gold nanostructures/graphene oxide composites via a one-pot green fabrication protocol and their interesting two-stage catalytic behaviors, *RSC Adv.* 7 (2017) 51838–51846, <https://doi.org/10.1039/C7RA11188F>.
- [16] R. Rajalakshmi, A. Rebekah, C. Viswanathan, N. Ponpandian, Evolution of intrinsic 1-3D WO₃ nanostructures: Tailoring their phase structure and morphology for robust hydrogen evolution reaction, *Chem. Eng. J.* 428 (2022), 132013, <https://doi.org/10.1016/J.CEJ.2021.132013>.
- [17] F.C. Tai, C. Wei, S.H. Chang, W.S. Chen, Raman and X-ray diffraction analysis on unburned carbon powder refined from fly ash, *J. Raman Spectrosc.* 41 (2010) 933–937, <https://doi.org/10.1002/jrs.2532>.
- [18] H. Long, T. Shi, H. Hu, S. Jiang, S. Xi, Z. Tang, Growth of hierachal mesoporous NiOnanosheets on carbon cloth as binder-free anodes for high-performance flexible lithium-ion batteries, *Sci. Rep.* 4 (2014) 7413, <https://doi.org/10.1038/srep07413>.
- [19] M.M. Mohamed, T.M. Salama, M.A. Hegazy, R.M. AbouShabba, S.H. Mohamed, Synthesis of hexagonal WO₃ nanocrystals with various morphologies and their enhanced electrocatalytic activities toward hydrogen evolution, *Int. J. Hydrog. Energy* 44 (2019) 4724–4736, <https://doi.org/10.1016/j.ijhydene.2018.12.218>.
- [20] S. Cong, Y. Yuan, Z. Chen, J. Hou, M. Yang, Y. Su, Y. Zhang, L. Li, Q. Li, F. Geng, Z. Zhao, Noble metal-comparable SERS enhancement from semiconducting metal oxides by making oxygen vacancies, *Nat. Commun.* 6 (2015) 7800, <https://doi.org/10.1038/ncomms8800>.
- [21] O. Akhavan, Bacteriorhodopsin as a superior substitute for hydrazine in chemical reduction of single-layer graphene oxide sheets, *Carbon N. Y* 81 (2015) 158–166, <https://doi.org/10.1016/j.carbon.2014.09.044>.
- [22] M.T. Camci, B. Ulugt, C. Kocabas, S. Suzer, In-Situ XPS monitoring and characterization of electrochemically prepared Au nanoparticles in an ionic liquid, *ACS Omega* 2 (2017) 478–486, <https://doi.org/10.1021/acsomega.6b00456>.
- [23] Y. Lv, Z. Chen, Y. Liu, T. Wang, Z. Ming, Oxygen vacancy improves the hydrogen evolution reaction property of WO₃-xnanosheets, *Nano-Struct. Nano-Objects* 15 (2018) 114–118, <https://doi.org/10.1016/j.nanoso.2017.08.017>.
- [24] A. Ali, P.K. Shen, Nonprecious metal's graphene-supported electrocatalysts for hydrogen evolution reaction: fundamentals to applications, *Carbon Energy* 2 (2020) 99–121, <https://doi.org/10.1002/cey.226>.
- [25] H. Darmstadt, L. Stummchen, U. Roland, C. Roy, S. Kaliaguine, A. Adnot, Surface vs. bulk chemistry of pyrolytic carbon blacks by SIMS and Raman spectroscopy, *Surf. Interface Anal.* 25 (1997) 245–253, [https://doi.org/10.1002/\(SICI\)1096-9918\(199704\)25:4<245::AID-SIA229>3.0.CO;2-U](https://doi.org/10.1002/(SICI)1096-9918(199704)25:4<245::AID-SIA229>3.0.CO;2-U).
- [26] D.K. Yadav, R. Gupta, V. Ganeshan, P.K. Sonkar, M. Yadav, Gold nanoparticles incorporated in a zinc-based metal-organic framework as multifunctional catalyst for the oxygen reduction and hydrogen evolution reactions, *ChemElectroChem* 5 (2018) 2612–2619, <https://doi.org/10.1002/celc.201800519>.
- [27] L. Najafi, S. Bellani, R. Oropesa-Nuñez, B. Martín-García, M. Prato, F. Bonaccorso, Single-/few-layer graphene as long-lasting electrocatalyst for hydrogen evolution reaction, *ACS Appl. Energy Mater.* 2 (2019) 5373–5379, <https://doi.org/10.1021/acsena.9b00949>.
- [28] L.L. Pesterfield, J.B. Maddox, M.S. Crocker, G.K. Schweitzer, Pourbaix (E–pH-M) diagrams in three dimensions, *J. Chem. Educ.* 89 (2012) 891–899, <https://doi.org/10.1021/ed200423n>.
- [29] Y. Chen, R. Ding, J. Li, J. Liu, Highly active atomically dispersed platinum-based electrocatalyst for hydrogen evolution reaction achieved by defect anchoring strategy, *Appl. Catal. B* 301 (2022), 120830, <https://doi.org/10.1016/j.apcatb.2021.120830>.
- [30] A. Lasia, Mechanism and kinetics of the hydrogen evolution reaction, *Int. J. Hydrog. Energy* 44 (2019), <https://doi.org/10.1016/j.ijhydene.2019.05.183>.
- [31] R. R, R. A, V. C, P. N, Evolution of intrinsic 1-3D WO₃ nanostructures: tailoring their phase structure and morphology for robust hydrogen evolution reaction, *Chem. Eng. J.* 428 (2022), 132013, <https://doi.org/10.1016/j.cej.2021.132013>.
- [32] A. Alobaid, C. Wang, R.A. Adomatish, Mechanism and kinetics of HER and OER on NiFe LDH films in an alkaline electrolyte, *J. Electrochem. Soc.* 165 (2018) J3395–J3404, <https://doi.org/10.1149/2.0481815jes>.
- [33] H.Q. Fu, M. Zhou, P.F. Liu, P. Liu, H. Yin, K.Z. Sun, H.G. Yang, M. Al-Mamun, P. Hu, H.-F. Wang, H. Zhao, Hydrogen spillover-bridged volmer/tafel processes enabling ampere-level current density alkaline hydrogen evolution reaction under low overpotential, *J. Am. Chem. Soc.* 144 (2022) 6028–6039, <https://doi.org/10.1021/jacs.2c01094>.
- [34] M. Xiong, Z. Gao, Y. Qin, Spillover in heterogeneous catalysis: new insights and opportunities, *ACS Catal.* 11 (2021) 3159–3172, <https://doi.org/10.1021/acscatal.0c05567>.
- [35] J. Chen, X. Wang, L. Zhang, Z. Rui, Strong metal-support interaction assisted redispersion strategy for obtaining ultrafine and stable IrO₂/Ir active sites with exceptional methane oxidation activity, *Appl. Catal. B* 297 (2021), 120410, <https://doi.org/10.1016/j.apcatb.2021.120410>.
- [36] J. Wang, X. Gu, L. Pei, P. Kong, J. Zhang, X. Wang, R. Wang, E.R. Waclawik, Z. Zheng, Strong metal-support interaction induced O₂ activation over Au/MnB₂O₆ (M = Zn²⁺, Ni²⁺ and Co²⁺) for efficient photocatalytic benzyl alcohol oxidative esterification, *Appl. Catal. B* 283 (2021), 119618, <https://doi.org/10.1016/j.apcatb.2020.119618>.
- [37] X. Wang, X. Li, D. Kong, L. Zhao, Y. Cui, Y. Wang, T. Cai, Q. Xue, Z. Yan, W. Xing, Platinum-free electrocatalysts for hydrogen oxidation reaction in alkaline media, *Nano Energy* (2022), 107877, <https://doi.org/10.1016/j.nanoen.2022.107877>.
- [38] S. Zhang, Z. Xia, M. Zhang, Y. Zou, H. Shen, J. Li, X. Chen, Y. Qu, Boosting selective hydrogenation through hydrogen spillover on supported-metal catalysts at room temperature, *Appl. Catal. B* 297 (2021), 120418, <https://doi.org/10.1016/j.apcatb.2021.120418>.
- [39] S. Stankovich, D.A. Dikin, R.D. Piner, K.A. Kohlhaas, A. Kleinhammes, Y. Jia, Y. Wu, S.T. Nguyen, R.S. Ruoff, Synthesis of graphene-based nanosheets via chemical reduction of exfoliated graphite oxide, *Carbon* 45 (2007) 1558–1565, <https://doi.org/10.1016/j.carbon.2007.02.034>.
- [40] T. Whittaker, K.B.S. Kumar, C. Peterson, M.N. Pollock, L.C. Grabow, B.D. Chandler, H₂ oxidation over supported Au nanoparticle catalysts: evidence for heterolytic H₂

- activation at the metal–support interface, *J. Am. Chem. Soc.* 140 (2018) 16469–16487, <https://doi.org/10.1021/jacs.8b04991>.
- [41] J. Zhang, H. Wang, L. Wang, S. Ali, C. Wang, L. Wang, X. Meng, B. Li, D.S. Su, F.-S. Xiao, Wet-chemistry strong metal–support interactions in titania-supported Au catalysts, *J. Am. Chem. Soc.* 141 (2019) 2975–2983, <https://doi.org/10.1021/jacs.8b10864>.
- [42] Q. Tang, D. Jiang, Mechanism of hydrogen evolution reaction on 1T-MoS₂ from first principles, *ACS Catal.* 6 (2016) 4953–4961, <https://doi.org/10.1021/acscatal.6b01211>.
- [43] J. Dai, Y. Zhu, Y. Chen, X. Wen, M. Long, X. Wu, Z. Hu, D. Guan, X. Wang, C. Zhou, Q. Lin, Y. Sun, S.-C. Weng, H. Wang, W. Zhou, Z. Shao, Hydrogen spillover in complex oxide multifunctional sites improves acidic hydrogen evolution electrocatalysis, *Nat. Commun.* 13 (2022) 1189, <https://doi.org/10.1038/s41467-022-28843-2>.
- [44] A. Kostuch, S. Jarzynski, M.K. Surówka, P. Kustrowski, Z. Sojka, K. Kruczala, The joint effect of electrical conductivity and surface oxygen functionalities of carbon supports on the oxygen reduction reaction studied over bare supports and Mn–Co spinel/carbon catalysts in alkaline media, *Catal. Sci. Technol.* 11 (2021) 7578–7591, <https://doi.org/10.1039/D1CY01115D>.
- [45] L. Warczinski, C. Hättig, How nitrogen doping affects hydrogen spillover on carbon-supported pd nanoparticles: new insights from DFT, *J. Phys. Chem. C* 125 (2021) 9020–9031, <https://doi.org/10.1021/acs.jpcc.0c11412>.
- [46] M. Vasilopoulou, A. Soulati, D.G. Georgiadou, T. Stergiopoulos, L.C. Palilis, S. Kennou, N.A. Stathopoulos, D. Davazoglou, P. Argitis, Hydrogenated under-stoichiometric tungsten oxide anode interlayers for efficient and stable organic photovoltaics, *J. Mater. Chem. A Mater. 2* (2014) 1738–1749, <https://doi.org/10.1039/c3ta13975a>.
- [47] R. Sharifian, R.M. Wagterveld, I.A. Digdaya, C. Xiang, D.A. Vermaas, Electrochemical carbon dioxide capture to close the carbon cycle, *Energy Environ. Sci.* 14 (2021) 781–814, <https://doi.org/10.1039/D0EE03382K>.
- [48] J.P. Meyers, R.M. Darling, Model of carbon corrosion in PEM fuel cells, *J. Electrochem Soc.* 153 (2006) A1432, <https://doi.org/10.1149/1.2203811>.
- [49] G. Mineo, M. Scuderi, E. Bruno, S. Mirabella, Engineering hexagonal/monoclinic WO₃ phase junctions for improved electrochemical hydrogen evolution reaction, *ACS Appl. Energy Mater.* 5 (2022) 9702–9710, <https://doi.org/10.1021/acsaem.2c01383>.